Spectral longwave atmospheric irradiance determination for site- and date-specific passive radiative cooling modeling

Sustainable Energy Technologies and Assessments 91 (2026) 105046

Contents lists available at ScienceDirect

Sustainable Energy Technologies and Assessments

journal homepage: www.elsevier.com/locate/seta

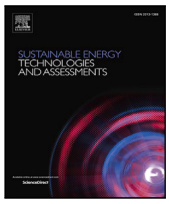

Original article

Spectral longwave atmospheric irradiance determination for site- and date-specific passive radiative cooling modeling

Claudio Belotti [a,*], Jochen Manara [b], Stephan Vidi [b], Lorenzo Pattelli [c], Jacques Hameury [d]

[a] Istituto Nazionale di Ottica (CNR-INO), Via Madonna del Piano 10, Sesto Fiorentino, Firenze, 50019, Italy
[b] Center for Applied Energy Research (CAE), Magdalene-Schoch-Str. 3, Wuerzburg, 97074, Germany
[c] Istituto Nazionale di Ricerca Metrologica (INRiM), Strada delle Cacce 91, Torino, 10135, Italy
[d] Laboratoire National de Métrologie et D'essais (LNE), 29, Avenue Roger Hennequin, Trappes Cedex, 78190, France

ARTICLE INFO

Dataset link: https://zenodo.org/records/17227622

Keywords:
Passive radiative cooling
Downwelling longwave atmospheric irradiance
Surface downward thermal radiation
ERA5 reanalysis
Radiative transfer modeling
Typical Meteorological Year
Thermal energy balance modeling

ABSTRACT

The effectiveness of passive radiative cooling is highly dependent on local atmospheric conditions, particularly the spectral distribution of downward longwave radiation. Many existing models rely on simplified or generalized assumptions such as fixed atmospheric profiles or empirical fits based on surface-level parameters that overlook important aspects of the vertical composition and spectral variability of the atmospheric column. In this work, we present a python-based workflow that generates site- and time-specific estimates of surface downward thermal radiation resolved into sixteen longwave spectral bands with hourly resolution. Our method combines reanalysis data from open ECMWF ERA5 and seasonal climatology data, and the RRTM_LW radiative transfer model, allowing for consistent incorporation of cloud effects based on the available input data. We demonstrate the application of this tool by constructing spectrally resolved Typical Meteorological Year (TMY) datasets and show how it can be used to improve energy balance calculations for radiative coolers. Comparisons with simplified approaches highlight the systematic errors arising when spectral and vertical atmospheric information are neglected.

Introduction

Radiative cooling technologies, and in particular passive daytime radiative cooling materials (PDRC), exploit the transparency of the Earth's atmosphere within the infrared "atmospheric transparency window" (approximately 8 μm–13 μm) to dissipate thermal energy to outer space and generate a net cooling power with no energy consumption. Evaluating the potential cooling power density generated at the surface of a PDRC system requires knowledge of the spectral solar irradiance on the surface, of the convective heat flux density, of the radiation heat flux density emitted by the surface toward the atmosphere and space, and of the radiation downwelling from the atmosphere that is absorbed onto the surface. Among all these factors, the latter is particularly challenging because it relies on the properties of the whole atmospheric column which are not easily measured. For this reason, most practical assessments of PDRC performance still rely on simplified representation of atmospheric radiative transfer, commonly assuming a uniform "sky temperature" or fixed "effective atmospheric transmissivity" which ignore the full vertical and spectral complexity of the atmosphere, leading to inaccuracies in the prediction of cooling power under specific application conditions.

Several empirical or semi-empirical models have been proposed to correct for these simplifications due to their relative simplicity and modest computational requirements. Commonly used relationships or look-up tables include those proposed by Idso [1] or Das and Iqbal [2], which however neglect vertical variations in atmospheric composition and temperature, using surface-level meteorological parameters to extrapolate atmospheric properties [3]. Notably, the Das and Iqbal [2] has been reported to yield spectral irradiances within parts of the atmospheric window that are less than half of observed values, likely due to differences in the absorption data used for atmospheric constituents [3]. For instance, local precipitable water vapor has been commonly adopted as a proxy for atmospheric emissivity or transmittance, particularly under clear-sky conditions [4,5]. However, these models typically neglect the vertical structure of the atmosphere and omit important radiatively active species such as CO_2 or O_3 as well as clouds and aerosols [6,7]. Additionally, they are not readily scalable for global assessment or for long-term performance evaluations across different years and climates, as they require the availability of measured meteorological data relative to the date and site of each experiment.

* Corresponding author.
E-mail address: claudio.belotti@cnr.it (C. Belotti).

https://doi.org/10.1016/j.seta.2026.105046
Received 30 September 2025; Received in revised form 27 March 2026; Accepted 17 May 2026
Available online 29 May 2026

Cloudy-sky conditions introduce further complexity. While many studies either neglect clouds entirely or treat their effects using simple scalar corrections based on cloud cover fraction [8], such empirical approaches often fail to capture the thermodynamic and vertical structure of cloud layers. Yet, especially in the context of passive radiative cooling, the correct modeling of clouds is paramount, since clouds can both obstruct access to the cold sky or themselves act as a radiative heat sink depending on their altitude, temperature, and phase. To address these aspects, recent works have either assumed a fixed cloud temperature [9] or proposed an empirical height-dependent cloud temperature model based on a fixed temperature difference scale [6] or a fixed atmospheric lapse rate [10]. While these studies raised awareness of the variable role of clouds in shaping downward longwave irradiance, they still rely on static or empirical assumptions regarding cloud height and temperature, and cannot capture the presence of multiple cloud layers, their vertical overlap, phase, or time- and location-specific evolution.

Compared to empirical models, observational datasets derived from satellite missions such as CERES [11] or MODIS-derived ELITE [12] provide high-quality estimates of surface longwave downwelling radiation, yet only as spectrally integrated totals [13]. Spectrally resolved irradiance datasets with comprehensive spatial and temporal coverage remain unavailable, which severely limits the accurate performance evaluation of spectrally selective radiative cooling surfaces.

To overcome these limitations, several researchers started using radiative transfer models such as MODTRAN [14–16], which allow for more detailed treatment of gas absorption. Radiative transfer models are widely applied in climate science, remote sensing and meteorology [17–23], but their integration into PDRC studies has remained relatively limited due to the high computational burden, lack of automation and difficulty in accessing appropriate input data on the local atmospheric composition.

Recent studies have attempted to bridge this gap by combining reanalysis datasets with radiative transfer calculations. For instance, Yang et al. [16] used total precipitable water vapor from the European Centre for Medium-Range Weather Forecasts (ECMWF) to parametrize spectral emissivity in MODTRAN, while adjusting for cloud height via empirical corrections. However, this approach remains constrained by the limited number of meteorological stations from the EnergyPlus database, and did not take full advantage of the vertical resolution available in reanalysis data. Similarly, Wu et al. [24] used ERA5 data to construct a (>50 GB) global Typical Meteorological Year (TMY) database, which however offers limited flexibility in terms of user-specific or on-demand evaluations.

Other works relied instead on commercial software (e.g., Meteonorm) [15,25], which however provides only spectrally integrated atmospheric data, lacking the spectral information required for the evaluation of radiative cooling surfaces that are explicitly designed for wavelength-selective emissivity profiles [26].

In general, several studies have shown that using only surface-level parameters such as ambient temperature or relative humidity leads to overestimated longwave downward radiation [6,27] and ultimately sky temperature models that are inaccurate for spectrally-selective materials [28]. As a matter of fact, besides the important spectral resolution, more recent studies have further stressed the importance of accounting for vertical gradients in the atmospheric composition and temperature [7,29,30]. For example, Mandal et al. [29] introduced a temperature correction to account for the colder upper atmosphere, but this approach remains applicable only under clear-sky conditions and cannot handle cloud effects.

Finally, spatial and temporal coverage of existing assessments remains an issue, with most approaches being limited to individual cities [16] which may not be representative of larger areas.

In this work, we present a method that combines full-resolution global reanalysis data from ECMWF ERA5 with the efficient RRTM_LW radiative transfer model developed by the Atmospheric and Environmental Research (AER) group to generate spectrally resolved longwave irradiance across 16 discrete bands [31,32]. This development was carried out within the EU project PaRaMetriC [33], aimed at establishing a metrological framework for the comparable performance evaluation of passive radiative cooling technologies.

The proposed approach, named *PaRaMetriC Atmospheric Spectral Tool for Irradiance Calculation using Hourly ERA5 data* (PASTICHE), preserves the full vertical structure of the atmospheric column, including pressure levels and gas concentrations, and supports modeling under both clear- and cloudy-sky conditions while avoiding the computational burden of line-by-line models.

Exploiting the globally available, hourly-resolved ERA5 dataset (1940–present) enables scalable and consistent assessment of radiative cooling performance across time and space. As an example application, we demonstrate the generation of on-demand TMY datasets for user-specified locations, using the PVGIS definition, while significantly reducing data transfer and storage needs compared to full TMY archives. The modeling pipeline is illustrated via a Jupyter notebook, making the entire framework open, accessible and reproducible, in contrast with several previous approaches based on commercial or closed-source software tools.

By making this tool available to the community studying PDRC and radiative heat exchange phenomena in general, we aim to support more accurate, comparable and location-specific assessment of radiative cooling performance under present-day and historical atmospheric conditions.

Methodology

Modeling of the Surface Downward Longwave Radiation (SDLR)

This section describes the methodology used to model site- and date-specific, spectrally-resolved hemispherical irradiance at the surface. To this end, we developed a software framework that encapsulates the entire process of obtaining spectral irradiance: from receiving the atmospheric state data and integrating it with ancillary sources, to simulating the downward surface radiation resolved by spectral band through a third-party model, and finally packaging the results into a file format suitable for use by end users. The software, named PASTICHE is released as open-source under the GPL-3.0 license and is available in an online repository [34]. An overview of the workflow is provided in Fig. 1. RRTM_LW is a widely established radiative transfer model that computes spectrally binned longwave radiative fluxes using a layered atmospheric description and a correlated-k approximation for gaseous absorption [35]. PASTICHE translates ERA5-derived atmospheric profiles and cloud properties into RRTM_LW inputs, while additional gas species are specified using standard RRTM presets and climatological data [36].

Routinely monitoring spectral SDLR is currently feasible only at a limited number of sites [37], primarily due to the need for sophisticated instrumentation [38]. Moreover, the instruments currently in use typically cover a restricted spectral range, often excluding the far-infrared region (wavelengths longer than 15 μm) [39,40]. Consequently, the absence of direct measurements must inevitably be addressed through atmospheric radiative transfer modeling.

The Longwave Rapid Radiative Transfer Model (RRTM_LW) [31] calculates the fluxes (irradiance) along the vertical dimension and on sixteen contiguous bands in the longwave (infrared) from 3 to 1000 μm in wavelength, details on RRTM spectral bands are summarized in Table 1. RRTM was selected for this study taking into account the availability of the code [32], the presence of scientific validation studies [23,31], its application into several general circulation models and the necessary compromise between accuracy and computational efficiency.

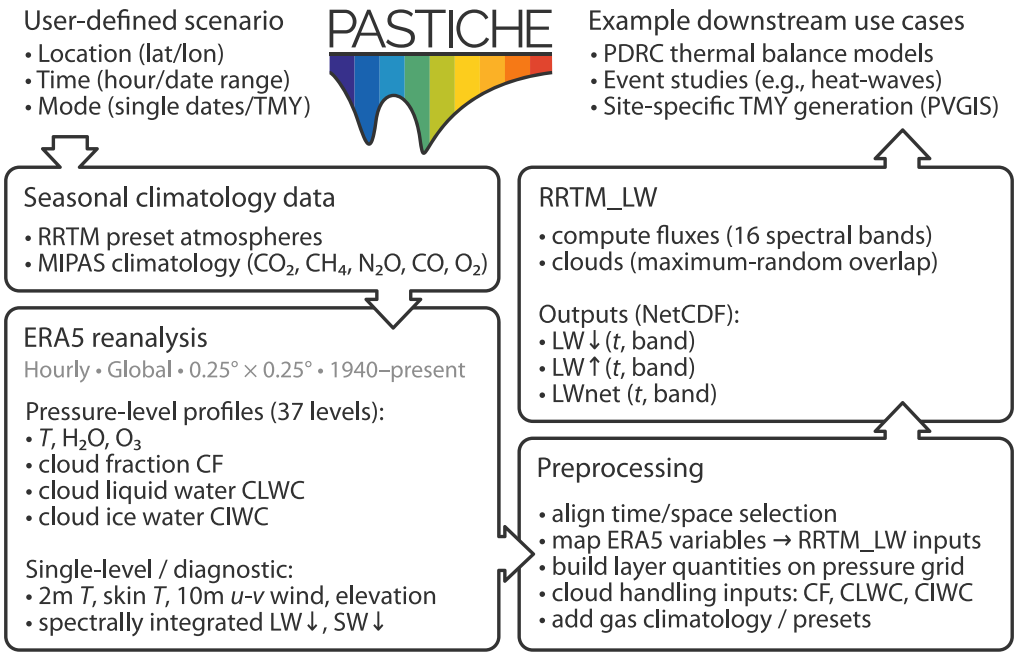

Fig. 1. Workflow schematic for the PASTICHE framework. The framework computes downward irradiance by running the RRTM radiative transfer model for a user-specified scenario. Atmospheric inputs include temperature, water vapor, ozone, and cloud parameters from ERA5, while additional species (e.g., CO_2, CH_4, O_2) are obtained from climatological datasets. Cloud overlap is handled using the maximum-random overlap scheme.

Table 1
Spectral bands and dominant absorbing gases for RRTM_LW. The primary atmospheric transparency window (8 μm to 13 μm) is resolved by multiple bands (Bands 5–9), including the ozone absorption band within this region (Band 7).

Band	Wavenumber range [cm^{-1}]		Wavelength range [μm]		Dominant absorbers
1	10	350	1000.0	28.6	H_2O
2	350	500	28.6	20.0	H_2O
3	500	630	20.0	15.9	H_2O, CO_2
4	630	700	15.9	14.3	H_2O, CO_2
5	700	820	14.3	12.2	H_2O, CO_2
6	820	980	12.2	10.2	H_2O
7	980	1080	10.2	9.3	H_2O, O_3
8	1080	1180	9.3	8.5	H_2O
9	1180	1390	8.5	7.2	H_2O, CH_4
10	1390	1480	7.2	6.8	H_2O
11	1480	1800	6.8	5.6	H_2O
12	1800	2080	5.6	4.8	H_2O, CO_2
13	2080	2250	4.8	4.4	H_2O, N_2O
14	2250	2380	4.4	4.2	CO_2
15	2380	2600	4.2	3.8	–
16	2600	3250	3.8	3.1	–

The model requires as input the state of the atmosphere, described by the temperature and pressure variation with altitude, gas composition of air and the presence of liquid and ice clouds. Its accuracy is comparable [31] to slower, high resolution line-by-line models, which in turn can attain an overall accuracy within $2\,W\,m^{-2}$ of observations [23].

In order to obtain a realistic calculation, the state of the atmosphere input to the model was defined from the ERA5 [41] reanalysis.

Reanalyses are datasets that combine observations and climate or numerical weather prediction model simulations of the past by means of data assimilation [42], they are coherent with the laws of physics and offer a detailed representation of atmospheric and surface conditions at regular intervals [43]. ERA5 dataset [44,45] spans from 1940 to the present, it provides hourly estimates for a large number of atmospheric and land-surface quantities, the data cover the Earth on a 0.25° latitude–longitude grid and divide the atmosphere in 37 pressure levels.

In particular, for each location and time-step at which the irradiance was calculated, the atmosphere was defined from the vertical distribution of temperature, water vapor, and ozone obtained from ERA5. Moreover, the specific cloud liquid water content and specific cloud ice water content profiles as well as the fraction of the reanalysis pixel covered by clouds at each height were used to simulate the radiative effect due to the presence of clouds. Finally, the values of concentration of the remaining molecular species required by RRTM: carbon dioxide, nitrous oxide, carbon monoxide, methane and molecular oxygen, were defined using the RRTM preset atmospheres and from a well-established latitudinally and seasonally-varying climatology [36].

Some of the sets covering a city, therefore a limited geographical area, were calculated over a 12-month period defined as a TMY, constructed by selecting representative months from multiple years to reflect average weather conditions. While the use of a TMY might not capture the current status and trend of climate change [46] — potentially introducing limitations in long-term energy performance assessments — it remains a widely accepted and standardized approach [47]. The months composing the TMY for each location were defined using PVGIS-ERA5 [48] which also based on ERA5 data from the 2005–2023 period, the variables used to select each typical month are global solar horizontal irradiance, air temperature, and relative humidity.

Thermal balance of a PDRC system

The heat fluxes acting at the surface of a PDRC emitter include the absorbed solar radiation, the infrared radiation absorbed from atmosphere, the radiative infrared flux emitted by the panel toward atmosphere and the convective flux.

The radiative power density emitted by the PDRC surface can be modeled as

$$Q_s = \pi \int_0^\infty \varepsilon_s(\lambda) I_b(\lambda, T_e) d\lambda = \int_0^\infty \varepsilon_s(\lambda) M_b(\lambda, T_e) d\lambda \quad (1)$$

with λ the wavelength, $\varepsilon_s(\lambda)$ the spectral normal emissivity of the panel surface, T_e the surface temperature of the panel and $I_b(\lambda, T_e)$, $M_b(\lambda, T_e)$ the spectral radiance of a blackbody and the hemispherical spectral emissive power of a blackbody at T_e, respectively. In Eq. (1), the spectral directional emissivity of the panel is assumed to be independent of direction. For an angular-dependent spectral directional emissivity the hemispherical spectral emissivity can be calculated using the usual equation given in [49], recalled in Eq. (B.1).

The radiative power density coming from the atmosphere and absorbed by the panel surface is modeled as:

$$Q_{atm} = \int_0^\infty \varepsilon_s(\lambda)\hat{q}_{atm}(\lambda)\mathrm{d}\lambda \tag{2}$$

with $\hat{q}_{atm}$ the hemispherical SDLR on the panel surface.

Considering the thermal balance on the surface of the PDRC material (incoming components are considered positive, while outgoing components are negative), the net heat flux density is given by relation [50]:

$$Q_{net} = -Q_s + Q_{atm} + Q_{sol} - Q_{conv} \quad \text{and} \quad Q_{net} = mc_p\frac{\mathrm{d}T}{\mathrm{d}t} \tag{3}$$

with Q_{sol} absorbed solar power density, Q_{conv} convective losses, and $mc_p\frac{dT}{dt}$ heat accumulation term. Q_{net} is positive when heat is gained by the PDRC system.

The absorbed solar power density is given by:

$$Q_{sol} = \int_0^\infty \int_{2\pi} \alpha_s(\lambda) i_{sol}(\lambda)\cos(\theta)\mathrm{d}\Omega\,\mathrm{d}\lambda = \int_0^\infty \int_{2\pi} \varepsilon_s(\lambda) i_{sol}(\lambda)\cos(\theta)\mathrm{d}\Omega\,\mathrm{d}\lambda \tag{4}$$

with $\alpha_s(\lambda)$ directional spectral absorptance, i_{sol} directional spectral density of radiance of incident solar radiation.

The convective losses are derived from the convective heat transfer coefficient h_{conv} calculated from the wind speed v_w according to [51] and see also Eqs. (B.2) and (B.3).

Hemispherical emissivity and solar absorptance

For determining the spectral near-normal emissivity $\varepsilon_n(\lambda)$ or absorptance $\alpha_n(\lambda)$, respectively, the spectral directional-hemispherical reflectance R_{dh} near-normal to the surface has been measured using an integrating sphere setup. For the solar spectral region an integrating sphere with an interior polytetrafluoroethylene surface and an UV/VIS/NIR diffraction spectrometer has been used. For the MIR wavelength range an integrating sphere with an interior gold surface and a FTIR-spectrometer has been used [52]. The total near-normal emissivity ε_n gives the total amount of thermal radiation that is emitted or absorbed by the surface nearly perpendicular to its orientation. The total near-normal emissivity ε_n with respect to the temperature T can be calculated by integrating the spectral near-normal emissivity ε_n over all wavelengths with the Planck-function $I_b(\lambda, T)$ as a weight function [49]:

$$\varepsilon_n(T) = \frac{\int_{3.1\,\mu m}^{1000\,\mu m} \varepsilon_n(\lambda) I_b(\lambda, T)\mathrm{d}\lambda}{\int_{3.1\,\mu m}^{1000\,\mu m} I_b(\lambda, T)\mathrm{d}\lambda} \tag{5}$$

The Planck-function $I_b(\lambda, T)$ gives the spectral intensity emitted by a black body at a certain temperature T. The calculations are done in accordance with DIN EN 12898 [53]. Finally, the total hemispherical emissivity ε_h can be calculated from the total near-normal emissivity ε_n following the formula given in DIN EN 12898 and recalled in Eq. (B.4).

Furthermore these calculations can be performed for the respective wavelengths bands, which are used in the atmospheric models by adapting the integration limits in Eq. (5) to the respective bands given in Table 1.

The solar absorptance α_{sol} is calculated, in accordance with DIN EN 410 [54], by integrating the spectral near-normal absorptance $\alpha_{\lambda,n}$ over the solar spectrum range with the solar radiation onto the soil I_{sol} as weight function as recalled in Eq. (B.5).

Results and validation

Model results

The spectral dimension of SDLR provides insight into various atmospheric processes that modulate its values. Spectral regions where the atmosphere exhibits higher opacity are particularly sensitive to variations in the state of tropospheric atmospheric layers. In contrast, the transparency of the so-called atmospheric window (780 cm^{-1} to 1250 cm^{-1}) results in very low SDLR values under clear-sky conditions, as the surface effectively observes the cold background of outer space. This behavior changes in the presence of clouds, which emit radiation at the temperature of the cloud layer itself, thereby increasing SDLR values within this spectral range.

An example of the output generated by the software discussed in Section "Modeling of the Surface Downward Longwave Radiation (SDLR)" is presented in Fig. 2, which displays a time series of atmospheric and meteorological variables for the city of Paris during June 2015, corresponding to the TMY month of June. The top panel illustrates the spectral SDLR as a color map with the spectral dimension represented along the y-axis. A recurring diurnal pattern is evident across several spectral bands, particularly below 630 cm^{-1} and within the range 1480 cm^{-1} to 1800 cm^{-1}, reflecting variations in temperature and humidity. In contrast, within the atmospheric transparency window, the influence of cloud cover is evident, resulting in increased values of SDLR.

The four lower panels display meteorological data obtained or derived from ERA5 for four grid boxes surrounding Paris. From bottom to top, these include cloud fraction (the percentage of each grid box covered by clouds), relative humidity, temperature of air at 2 m above the surface, and incoming solar radiation. All panels share a common x-axis, representing time (days in June TMY).

Results for multiple global locations, covering entire TMY periods as well as shorter time spans associated with heatwave events, are accessible under the Zenodo community page of the PaRaMetriC project [55].

Model validation

Building on RRTM extensive validation in dedicated studies [23,31] against the Line-By-Line Radiative Transfer Model (LBLRTM) [56], which itself has demonstrated high accuracy through numerous comparisons with observational measurements [57], here we present a comparison of our radiative calculations with both ERA5 total fluxes and ground-based Baseline Surface Radiation Network (BSRN) measurements [58] to assess the performance of PASTICHE in reproducing atmospheric radiative properties.

Table A.1 reports the validation metrics (correlation, bias, RMSE) used to quantify the differences between the SDLR, integrated over the spectral range, and the corresponding variable from ERA5 for multiple global locations over a whole TMY.

Discrepancies between the integrated irradiance results from PASTICHE and those from ERA5 can be attributed to several factors. First, the radiative transfer models differ: while the ECMWF IFS radiation scheme previously relied on RRTM [59], the current version employs ECRAD [60]. Second, PASTICHE's treatment of cloud effects relies on the cloud parameters available in ERA5, which do not include detailed microphysical data (e.g., particle effective radii). This may introduce differences in cloud-related radiative contributions. Third, aerosol effects were excluded from the PASTICHE simulations because of the technical challenges of incorporating them into RRTM. Finally, ERA5 employs a high vertical resolution with 137 model levels, whereas the publicly available data are provided on a coarser grid of 37 standard pressure levels, potentially affecting the accuracy of radiative flux results.

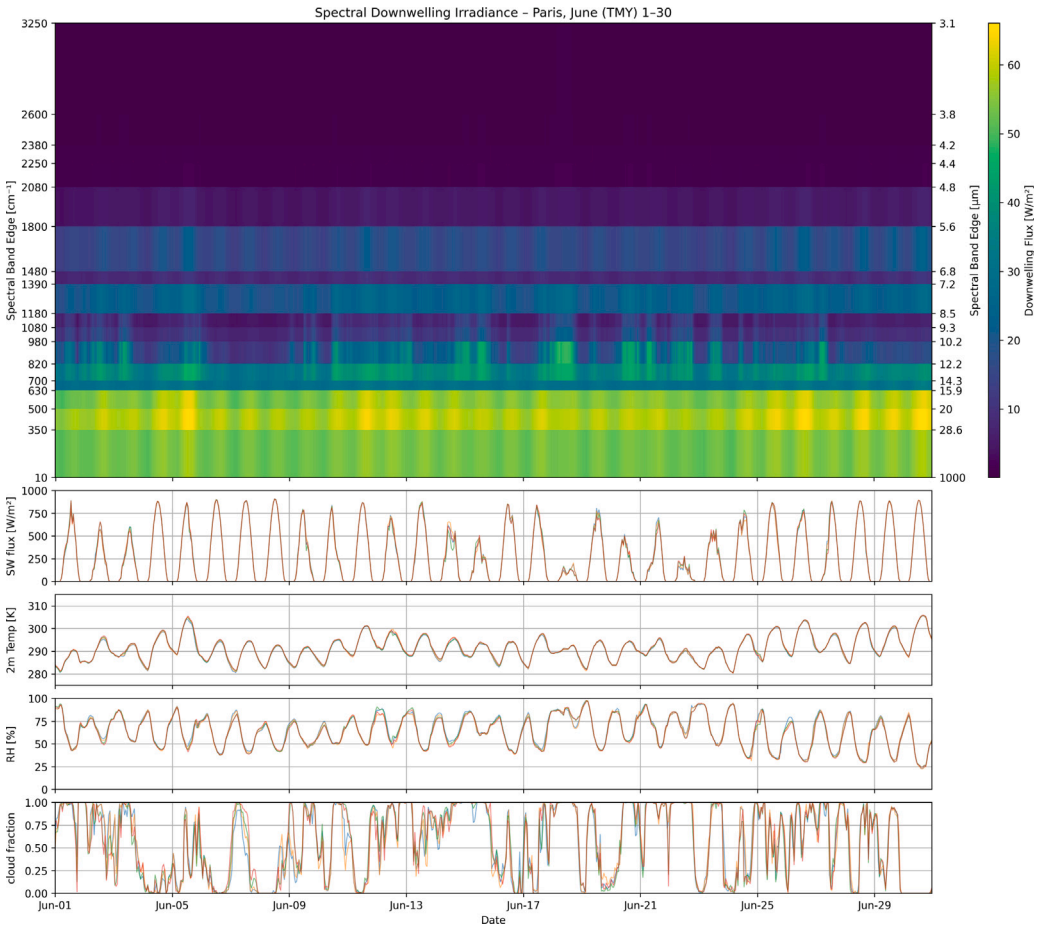

Fig. 2. Paris June TMY time series showing spectral irradiance and various meteorological variables. All panels share a common x-axis representing time (days in June TMY). Top panel: atmospheric spectral irradiance, averaged over the whole city area, with the left y-axis showing wavenumber and the right y-axis showing wavelength. The remaining panels display corresponding atmospheric data, either downloaded or derived from ERA5, for each of the four grid boxes. From bottom to top: cloud fraction (percentage of the grid box covered by clouds), relative humidity, 2-meter air temperature, and shortwave flux (solar radiation).

To contextualize the tabulated metrics, Fig. 3 displays two-dimensional histograms comparing the spectrally integrated SDLR (y-axis) with the corresponding ERA5 values (x-axis) for Paris over the entire TMY period. The left-hand panel illustrates the density of data points within each bin, providing a visualization of the distribution and agreement between the two datasets. The dataset comprises 35 026 data points, derived from 4 grid points, sampled hourly over 365 days. The correlation between the datasets is 0.95, with a negative bias of $-5.7\,\mathrm{W\,m^{-2}}$, and an RMSE of $13.8\,\mathrm{W\,m^{-2}}$. Notably, the small negative bias values are consistent with the effect expected from including aerosols [61]—which are accounted for in the ERA5 fluxes, but not included at the moment in the RRTM_LW workflow. The histograms indicate that the vast majority of data fall within bins aligned along the Cartesian diagonal. In contrast, the right-hand panel examines cloud influence, depicting the same data color-coded by ERA5 cloud fraction. Pixels with cloud fractions higher than 0.5, tend to deviate further from the 1:1 diagonal; in particular, for PASTICHE, the most overcast pixels exhibit higher SDLR values than those in ERA5. However, the left-hand panel confirms that these bins contain very few data points.

In addition to validation against reanalysis data, ground-based measurements were sought to validate the results against field observations. The Palaiseau SIRTA Observatory BSRN station (PAL, latitude 48.713°N, longitude 2.208°E) [62] is located near one of the locations selected for the PaRaMetriC project (Paris), approximately 5 km from the ERA5 grid point centered at 48.75°N, 2.25°E. The station measures SDLR together with additional parameters at 1-minute intervals. Hourly averages were created from the PAL time series for comparison with the corresponding grid point.

The comparison metrics for PASTICHE versus BSRN measurements are reported in Table A.2 for each TMY month and the whole TMY. Annually, the correlation between the datasets is 0.88, with a negative bias of $-8.6\,\mathrm{W\,m^{-2}}$ and an RMSE of $21.0\,\mathrm{W\,m^{-2}}$; these values are comparable to previous studies [63–65]. The comparison is also contextualized in Fig. A.1, which contrasts the spectrally integrated SDLR against BSRN radiation measurements. It is worth noting, however, that single observation stations might not be representative of the areal mean of a grid-level product, even when the station is located near the center of the grid cell [66]. Indeed, comparing ERA5 SDLR to the PAL dataset yields similar values for correlation and RMSE, 0.86 and $21.2\,\mathrm{W\,m^{-2}}$, respectively, although with a lower mean bias of $-2.4\,\mathrm{W\,m^{-2}}$, as reported in Table A.2 and Fig. A.2.

To examine temporal variability, Fig. 4 shows the time series of the spectrally integrated SDLR (green line), ERA5 all-sky dataset (blue), and BSRN measurements for the Paris grid point containing the PAL station for June 2015. Overall, the calculated values closely follow the temporal evolution of the ERA5 dataset, with differences averaging -1 %, though some discrepancies are apparent during cloudy intervals. The temporal variability of the BSRN time series is qualitatively consistent with the other datasets, although it exhibits more pronounced differences in both absolute values and fine temporal evolution. The lower panel quantifies these differences by displaying the percentage deviations between the datasets.

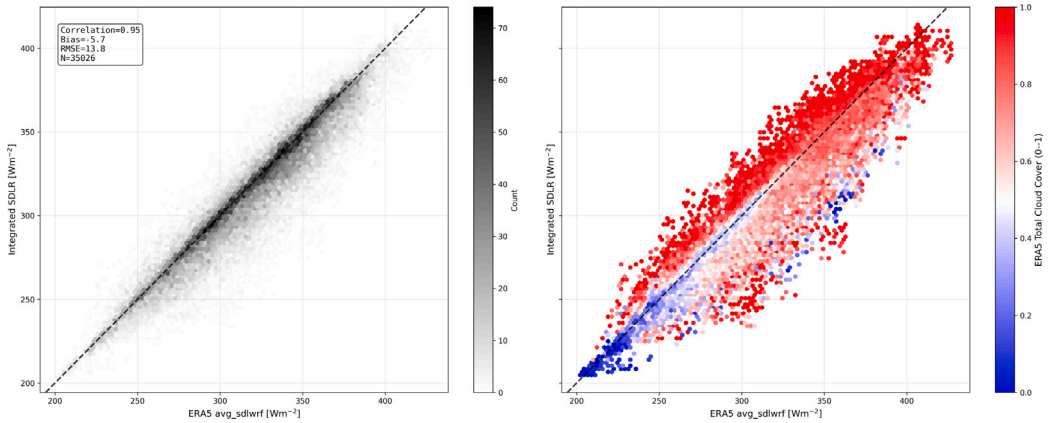

Fig. 3. 2D histogram plots of data for Paris, whole TMY, showing the spectrally integrated Surface Downward Longwave Radiation calculated as in Section "Modeling of the Surface Downward Longwave Radiation (SDLR)" (y-axis) and the same quantity from the ERA5 product (x-axis). The left-hand side panel represents the density for each bin, the inset reports the values of correlation, bias, RMSE, and number of points. In the right-hand side panel, data are color-coded by the corresponding ERA5 cloud fraction.

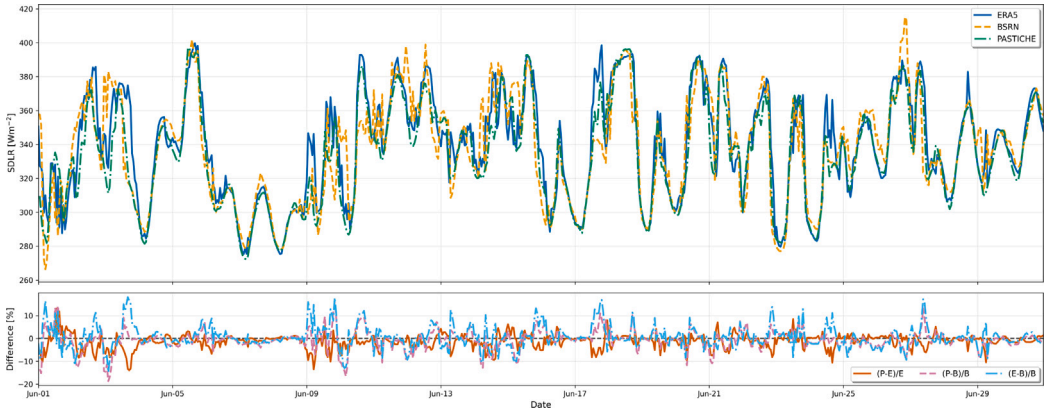

Fig. 4. Time series of Surface Downward Longwave Radiation for Paris during June (TMY). Upper panel: spectrally integrated DLR calculated as described in Section "Modeling of the Surface Downward Longwave Radiation (SDLR)" compared to ERA5 reanalysis all-sky product and ground-based measurements from the Palaiseau SIRTA Observatory station. Lower panel: Percentage differences between the three datasets PASTICHE (P), BSRN (B), and ERA5 (E).

Illustrative PDRC scenarios

As an illustrative application, results generated with PASTICHE are used to simulate the radiative cooling effects of a PRC surface following the methodology described in Section "Thermal balance of a PDRC system". The simulations are presented for the month of June in Paris and are intended to demonstrate how site- and date-specific, spectrally resolved atmospheric irradiance data can be used in practice.

Two scenarios are considered. In the first scenario, the PRC surface is treated as massless and its temperature is constrained to be equal to the ambient air temperature. In this case, only radiative heat fluxes are evaluated. In the second scenario, the PRC surface is assumed to be applied on top of a 5 cm thick concrete slab with a specific heat capacity of $1000\,\mathrm{J\,kg^{-1}\,K^{-1}}$ and a density of $2200\,\mathrm{kg\,m^{-3}}$. The backside of the slab is assumed to be adiabatic, allowing the surface temperature to vary dynamically in response to climatic conditions and the associated heat fluxes appearing in Eq. (3). In this second scenario, convective heat transfer between the surface and ambient air is also considered.

For the massive case, the calculations are performed at each time step using a transient energy balance. The surface temperature $T_{\mathrm{surf},0}$ is initialized to the ambient temperature at time $t = 0$ and subsequently updated based on the net heat gains and losses at each time step according to Eq. (3).

For this illustrative example, we selected one of the PRC materials studied within the PaRaMetriC project. The material consists of a silver-based highly reflective substrate (VEGA98®, Almeco S.p.A.) coated with a thin polymeric layer with spectrally selective emissivity (Cooling Photonics S.L.). This composite PDRC material, referred to as V98RF, was characterized spectrally using a UV/VIS/NIR spectrometer and a FTIR-spectrometer, each equipped with an integrating sphere setup, as described above. For visualization purposes, the spectral hemispherical emissivity was derived from the measured spectral near-normal emissivity. The resulting spectral hemispherical emissivity is shown on the left side of Fig. 5 and is in excellent agreement with previous independent spectral characterization performed by the Physikalisch-Technische Bundesanstalt [67]. In Fig. 5, the measured spectral hemispherical emissivity is plotted as a blue line. The light gray areas visualize the solar irradiation onto the soil and the thermal radiation at ambient temperature, respectively. The hemispherical emissivity calculated for each RRTM_LW wavelength band is plotted as purple bars. The total hemispherical emissivity, obtained by integrating the spectral hemispherical emissivity over all wavelengths is 0.637 and is indicated by a green line for comparison. Additionally, the solar absorptance, calculated using Eq. (5), is 0.025 and is shown as a yellow line in Fig. 5.

The net surface heat gains or losses are calculated for both scenarios using the heat fluxes described in Section "Thermal balance of a PDRC system". In the massless scenario, convective heat transfer is omitted. Solar absorption and infrared emission are calculated using the measured emissivity data, the prescribed surface temperature, the incident

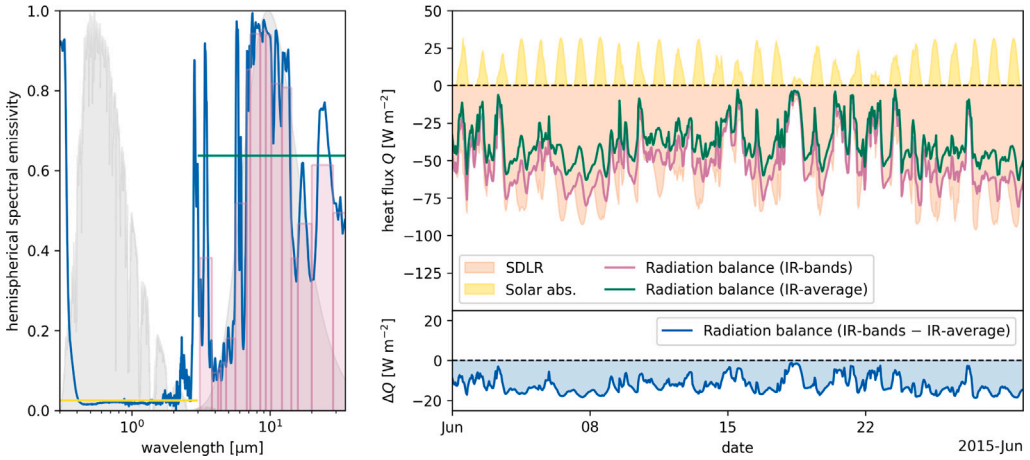

Fig. 5. Left: Measured spectral hemispherical emissivity of the V98RF surface (blue curve). The effective emissivity values for the solar and IR regions are indicated by the yellow and green lines, respectively. Purple bars represent the emissivity values for each IR band used in the proposed model. Top right: Heat flux components at the surface for the no-mass PRC surface. The resulting radiation balance is shown in purple for the calculation using the IR bands and in green for the calculation using the averaged IR emissivity (IR-total). Bottom right: Difference in radiation balance between band calculation and average value calculation.

solar irradiance, and the downward longwave irradiance provided by PASTICHE. Infrared fluxes are evaluated on a per-band basis (see Table 1). For the massive scenario, convective heat transfer is additionally estimated using ERA5 wind speed data together with surface and air temperatures. Ambient air temperature, solar irradiance, and wind speed are obtained from ERA5 reanalysis data.

The results for the massless scenario are shown on the right side of Fig. 5. The solar heat flux (yellow shading) and the net infrared heat flux (red shading) are shown, together with the resulting radiation balance (purple curve). For comparison, the radiation balance computed using a spectrally averaged hemispherical emissivity is shown as a green curve. The difference between the band-resolved and spectrally averaged radiation balances is reported in the lower-right panel of Fig. 5. The corresponding results for the massive scenario are shown on the left side of Fig. 6, where the solar, infrared, and convective heat fluxes are indicated by yellow, red, and blue shading, respectively. As in the massless case, the purple and green curves represent the band-resolved and spectrally averaged radiation balances, and their difference is shown in the lower-left panel. For context, we note that the net cooling fluxes obtained here for the massless, no-convection scenario in Paris are of the same order of magnitude as radiative cooling potentials reported in previous large-scale studies for this location, despite differences in modeling assumptions [25].

In the massive scenario, the inclusion of thermal mass allows the surface temperature to be computed from the net surface heat flux. The resulting surface temperature is compared with the ambient air temperature, and the corresponding average monthly cooling values for different locations are summarized on the right side of Fig. 6.

Conclusion

In this work, we introduced a method that combines full spatial resolution and hourly global reanalysis data with an efficient radiative transfer model to generate site- and date-specific, spectrally resolved longwave atmospheric irradiance. Unlike empirical or semi-empirical approaches that rely on surface-level parameters and spectrally averaged representations, the proposed framework preserves the complete vertical structure of the atmosphere and explicitly accounts for spectral variability and cloud effects, addressing key limitations of existing methods commonly used in passive radiative cooling studies.

Validation against ERA5-integrated longwave fluxes demonstrated strong agreement (correlation up to 0.98, RMSE $\approx 11\,\mathrm{W\,m^{-2}}$; see Table A.1 and Fig. 3), confirming the robustness of the ERA5-to-RRTM_LW data translation and the consistency of the resulting irradiance estimates. In addition, the integrated longwave irradiance estimates were found to be consistent with independent ground-based observations from the BSRN network.

Applying the model to the TMY datasets showed sub-ambient temperatures and therefore sub-ambient cooling of the investigated PDRC surface not only at night but also during the day. An illustrative application was presented to demonstrate how the spectrally resolved outputs provided by PASTICHE can be used in practice. By comparing band-resolved and spectrally averaged formulations under both massless and massive surface assumptions, the results highlight systematic differences in the resulting surface energy balance. Even under conservative conditions, differences on the order of $10\,\mathrm{W\,m^{-2}}$ to $20\,\mathrm{W\,m^{-2}}$ are observed for spectrally selective PDRC materials between band-based and averaged calculations, underscoring the importance of accounting for spectral effects when modeling radiative cooling performance. These results emphasize that the spectral structure of atmospheric longwave irradiance is not a secondary detail, but can lead to relevant deviations in predicted cooling fluxes if neglected. Additionally, given that one approach for improving PDRC surfaces is the selective increase of the spectral emissivity in the wavelength range of the atmospheric transparency window, this model supports the development and optimization of PDRC materials.

To encourage broader adoption, PASTICHE is made available as an open-source software framework that orchestrates data sourcing and interfaces with the radiative transfer model, enabling accurate, comparable, and location-specific assessments of radiative cooling performance. Its open implementation and reduced computational burden make it a practical and reproducible alternative to commercial or closed-source tools.

Recent studies have highlighted the relevance of radiative cooling in the context of climate change, both in terms of projected performance under future climates [25] and its potential role in large-scale climate mitigation strategies [68]. In principle, future climate scenarios could be explored by coupling projected atmospheric datasets with the present modeling framework; such extensions are left for future work.

Taken together, the methodological advances and open implementation presented in this work provide a scalable foundation for accurate, location-specific evaluation of radiative heat exchange involving sky-facing materials, the systematic investigation of spectral effects in radiative cooling applications, and their reproducible integration into energy and climate analyses.

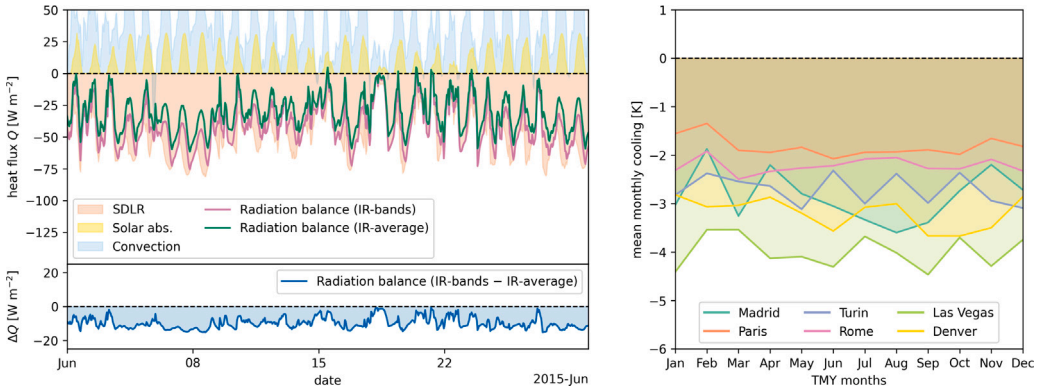

Fig. 6. Top left: Heat flux components at the surface for a PRC surface applied on top of a 5 cm thick slab of concrete. The resulting radiation balance is shown in purple for the calculation using the IR bands and in green for the calculation using the averaged IR emissivity (IR-average). Bottom left: Difference in radiation balance between band calculation and average value calculation. Right: Average monthly cooling effect for V98RF across multiple locations.

CRediT authorship contribution statement

Claudio Belotti: Writing – original draft, Visualization, Validation, Software, Methodology, Investigation, Data curation, Conceptualization. **Jochen Manara:** Writing – original draft, Methodology, Conceptualization. **Stephan Vidi:** Writing – original draft, Visualization, Validation, Software, Methodology, Conceptualization. **Lorenzo Pattelli:** Writing – original draft, Visualization, Supervision, Project administration, Conceptualization. **Jacques Hameury:** Writing – original draft, Supervision, Conceptualization.

Software availability

The source code is available from: https://github.com/21grd03-parametric/pastiche/

Declaration of competing interest

The authors declare that they have no known competing financial interests or personal relationships that could have appeared to influence the work reported in this paper.

Acknowledgments

This work is supported by the European project PaRaMetriC, code 21GRD03. The project 21GRD03 PaRaMetriC received funding from the European Partnership on Metrology, co-financed by the European Union's Horizon Europe Research and Innovation Programme, and from the Participating States.

Appendix A. Supplementary results of PASTICHE validation

Table A.1 reports validation metrics for several sites.

Additional results of the comparison between PASTICHE and BSRN PAL station observations are reported in Figs. A.1, A.2, and Table A.2.

Table A.1
Validation metrics for PASTICHE integrated SDLR for several locations over a whole TMY. N indicates the number of data points considered for each location.

Location	Corr.	Bias [W m^{-2}]	RMSE [W m^{-2}]	N
Denver	0.97	−2.7	12.0	78 807
Las Vegas	0.98	−4.7	10.9	78 825
Madrid	0.96	−3.6	11.4	175 146
Paris	0.95	−5.7	13.8	35 026
Rome	0.97	−3.7	11.5	34 967
Turin	0.96	−2.2	14.0	35 024

Appendix B. Detailed equations

For an angular-dependent spectral directional emissivity the hemispherical emissivity can be calculated by using the following equation:

$$\varepsilon_{\mathrm{h}}(\lambda) = \frac{1}{\pi}\int_{\mathrm{hem}} \varepsilon_{\mathrm{s}}(\lambda)\cos(\theta)\mathrm{d}\omega \tag{B.1}$$

with θ the angle to normal direction (zenith) and $\mathrm{d}\omega$ the differential element of solid angle.

The convective losses can be derived from the convective heat transfer coefficient h_{conv}:

$$Q_{\mathrm{conv}} = h_{\mathrm{conv}}(T_{\mathrm{s}} - T_{\mathrm{air}}) \tag{B.2}$$

The convective heat transfer coefficient was calculated from the wind speed v_{w} according to [51]:

$$h_{\mathrm{conv}} = 8.3 + 2.2v_{\mathrm{w}} \tag{B.3}$$

The total hemispherical emissivity ε_{h} can be calculated from the total near-normal emissivity ε_{n} following the formula given in DIN EN 12898:

$$\varepsilon_{\mathrm{h}} = 1.1887\varepsilon_{\mathrm{n}} - 0.4967\varepsilon_{\mathrm{n}}^2 + 0.2452\varepsilon_{\mathrm{n}}^3 \tag{B.4}$$

The solar absorptance α_{sol} is calculated by integrating the spectral near-normal absorptance $\alpha_{\lambda,n}$ over all wavelengths with the solar radiation onto the soil I_{sol} as weight function:

$$\alpha_{\mathrm{sol}} = \frac{\int_{0.3\,\mu\mathrm{m}}^{2.5\,\mu\mathrm{m}} \alpha_{\mathrm{n}}(\lambda) I_{\mathrm{sol}}(\lambda)\mathrm{d}\lambda}{\int_{0.3\,\mu\mathrm{m}}^{2.5\,\mu\mathrm{m}} I_{\mathrm{sol}}(\lambda)\mathrm{d}\lambda} \tag{B.5}$$

The calculations are done in accordance with DIN EN 410 [54].

Data availability

The data for this study is available from: https://zenodo.org/records/17227622.

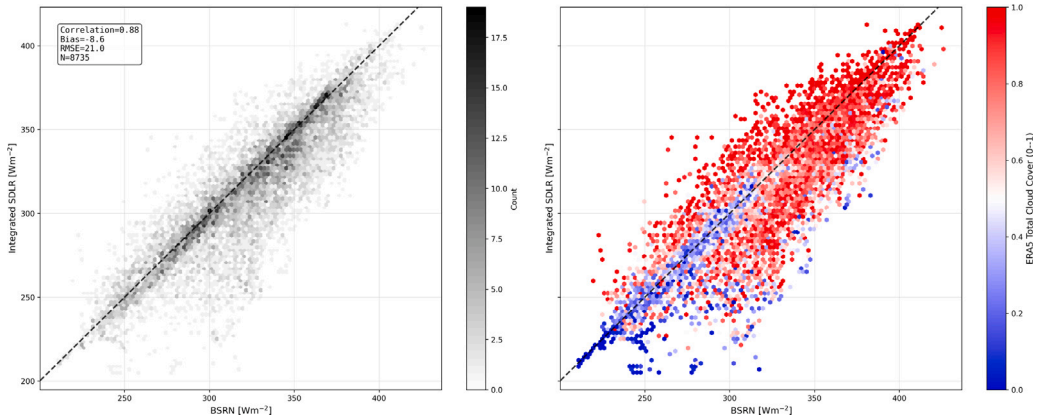

Fig. A.1. Same as Fig. 3, but showing the spectrally integrated Surface Downward Longwave Radiation calculated as in Section "Modeling of the Surface Downward Longwave Radiation (SDLR)" (*y*-axis) and the BSRN PAL measurements (*x*-axis). 2D histogram plots of data for Paris, whole TMY. The left-hand side panel represents the density for each bin, the inset reports the values of correlation, bias, RMSE, and number of points. In the right-hand side panel, data are color-coded by the corresponding ERA5 cloud fraction.

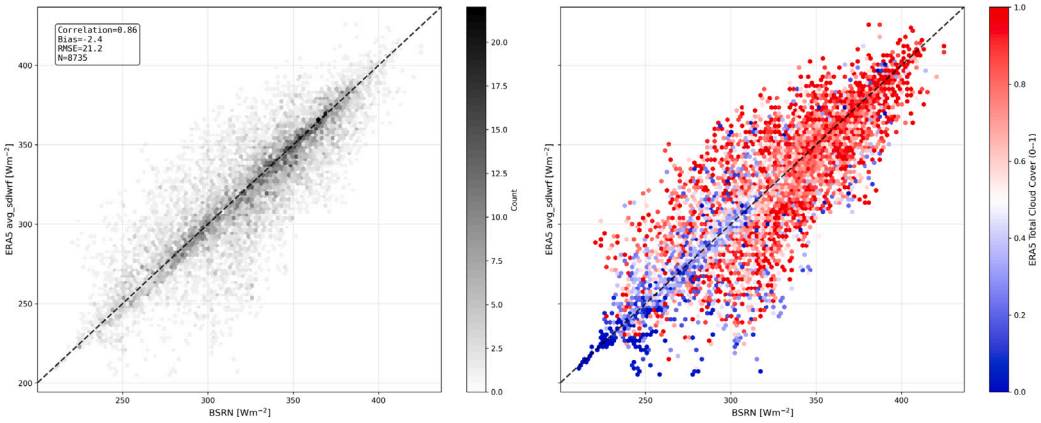

Fig. A.2. Same as Figs. 3 and A.1, but showing the spectrally integrated Surface Downward Longwave Radiation from the ERA5 product (*y*-axis) and the BSRN PAL measurements (*x*-axis). 2D histogram plots of data for Paris, whole TMY. The left-hand side panel represents the density for each bin, the inset reports the values of correlation, bias, RMSE, and number of points. In the right-hand side panel, data are color-coded by the corresponding ERA5 cloud fraction.

Table A.2
Monthly comparison statistics for PASTICHE vs. BSRN (P–B), PASTICHE vs. ERA5 (P–E), and ERA5 vs. BSRN (E–B) at PAL. *N* indicates the number of data points considered for each month.

	Correlation			Bias [W m^{-2}]			RMSE [W m^{-2}]			N
	P–B	P–E	E–B	P–B	P–E	E–B	P–B	P–E	E–B	
January	0.80	0.92	0.75	−12.3	−6.4	−6.0	27.2	16.6	27.0	744
February	0.93	0.96	0.91	−6.5	−4.7	−1.8	17.2	12.6	17.3	672
March	0.90	0.92	0.85	−6.3	−8.4	2.1	17.0	15.9	19.4	744
April	0.80	0.90	0.74	−5.7	−5.7	0.0	19.2	14.2	21.6	720
May	0.87	0.93	0.87	−5.0	−4.3	−0.6	18.0	12.9	17.7	744
June	0.89	0.94	0.86	−2.9	−4.7	1.7	14.8	11.8	16.3	720
July	0.85	0.92	0.82	−11.7	−5.7	−6.0	18.8	12.1	17.5	744
August	0.84	0.92	0.81	−6.6	−7.7	1.0	17.9	14.1	18.5	744
September	0.87	0.93	0.84	−5.6	−6.8	1.2	17.4	13.9	18.5	703
October	0.87	0.93	0.83	−5.5	−5.6	0.1	17.5	13.0	18.7	744
November	0.91	0.94	0.87	−9.2	−6.6	−2.6	20.0	15.4	21.6	720
December	0.67	0.92	0.67	−25.1	−7.4	−17.7	37.0	15.9	33.3	736
Annual	**0.88**	**0.95**	**0.86**	**−8.6**	**−6.2**	**−2.4**	**21.0**	**14.1**	**21.2**	**8735**

References

[1] Idso Sherwood B. A set of equations for full spectrum and 8- to 14-μ m and 10.5- to 12.5-μ m thermal radiation from cloudless skies. Water Resour Res 1981;17(2):295–304. http://dx.doi.org/10.1029/WR017i002p00295.

[2] Das AK, Iqbal M. A simplified technique to compute spectral atmospheric radiation. Sol Energy 1987;39(2):143–55. http://dx.doi.org/10.1016/S0038-092X(87)80042-7.

[3] Skartveit Arvid, Olseth Jan Asle, Czeplak Gerhard, Rommel Matthias. On the estimation of atmospheric radiation from surface meteorological data. Sol Energy 1996;56(4):349–59. http://dx.doi.org/10.1016/0038-092X(95)00117-A.

[4] Zhao Dongliang, Aili Ablimit, Zhai Yao, Lu Jiatao, Kidd Dillon, Tan Gang, Yin Xiaobo, Yang Ronggui. Subambient cooling of water: toward real-world applications of daytime radiative cooling. Joule 2019;3(1):111–23. http://dx.doi.org/10.1016/j.joule.2018.10.006.

[5] Zhu Yazhu, Qian Hua, Yang Ronggui, Zhao Dongliang. Radiative sky cooling potential maps of China based on atmospheric spectral emissivity. Sol Energy 2021;218:195–210. http://dx.doi.org/10.1016/j.solener.2021.02.050.

[6] Aili Ablimit, Yin Xiaobo, Yang Ronggui. Global radiative sky cooling potential adjusted for population density and cooling demand. Atmosphere 2021;12(11). http://dx.doi.org/10.3390/atmos12111379, URL https://www.mdpi.com/2073-4433/12/11/1379.

[7] Huang Jingyuan, Lin Chongjia, Li Yang, Huang Baoling. Effects of humidity, aerosol, and cloud on subambient radiative cooling. Int J Heat Mass Transfer 2022;186:122438. http://dx.doi.org/10.1016/j.ijheatmasstransfer.2021.122438, URL https://www.sciencedirect.com/science/article/pii/S0017931021015362.

[8] Wang Kaicun, Liang Shunlin. Global atmospheric downward longwave radiation over land surface under all-sky conditions from 1973 to 2008. J Geophys Res: Atmospheres 2009;114(D19). http://dx.doi.org/10.1029/2009JD011800.

[9] Seo Junyong, Choi Minwoo, Yoon Siwon, Lee Bong Jae. Climate-dependent optimization of radiative cooling structures for year-round cold energy harvesting. Renew Energy 2023;217:119166.

[10] Chen Hao, Wei Jia, Liu Xiangjun, Liu Jingchong, Wang Cunhai. Assessing radiative cooling power considering the cloud effects. Appl Therm Eng 2025;127192.

[11] Loeb Norman G, Doelling David R, Wang Hailan, Su Wenying, Nguyen Cathy, Corbett Joseph G, Liang Lusheng, Mitrescu Cristian, Rose Fred G, Kato Seiji. Clouds and the Earth's radiant energy system (CERES) energy balanced and filled (EBAF) Top-of-Atmosphere (TOA) Edition-4.0 Data product. J Clim 2018;31(2):895–918. http://dx.doi.org/10.1175/JCLI-D-17-0208.1, URL https://journals.ametsoc.org/view/journals/clim/31/2/jcli-d-17-0208.1.xml, Publisher: American Meteorological Society Section: Journal of Climate.

[12] Cheng Jie, Zeng Qi, Sun Hao, Yamin Guo, Yang Feng, Guo Mengfei, Wu Chenze. A global 1 km resolution daily surface longwave radiation product from MODIS satellite data from 2000–2023. Sci Data 2025;12(1):736. http://dx.doi.org/10.1038/s41597-025-05076-8, URL https://www.nature.com/articles/s41597-025-05076-8, Publisher: Nature Publishing Group.

[13] Yang Feng, Cheng Jie. A framework for estimating cloudy sky surface downward longwave radiation from the derived active and passive cloud property parameters. Remote Sens Environ 2020;248:111972.

[14] Li Mengying, Coimbra Carlos FM. On the effective spectral emissivity of clear skies and the radiative cooling potential of selectively designed materials. Int J Heat Mass Transfer 2019;135:1053–62. http://dx.doi.org/10.1016/j.ijheatmasstransfer.2019.02.040, URL https://www.sciencedirect.com/science/article/pii/S0017931018352566.

[15] Farooq Abdul Samad, Alkaabi Khaula, Hdhaiba Saif Bn. Exploring radiative sky cooling resource map and the impact of meteorological conditions on radiative emitters. a perspective of GCC countries. Energy Rep 2023;10:473–83. http://dx.doi.org/10.1016/j.egyr.2023.06.054, URL https://www.sciencedirect.com/science/article/pii/S2352484723010752.

[16] Yang Yujie, Zhang Guoqiang, Rong Li. Cooling energy savings from passive daytime radiative cooling in europe: A comparative analysis with and without population weighting from open-source data, with additional comparisons to Chinese cities. Energy Convers Manage 2024;314:118616. http://dx.doi.org/10.1016/j.enconman.2024.118616, URL https://www.sciencedirect.com/science/article/pii/S0196890424005570.

[17] Rothman Laurence S. History of the HITRAN database. Nat Rev Phys 2021;3(5):302–4. http://dx.doi.org/10.1038/s42254-021-00309-2, URL https://www.nature.com/articles/s42254-021-00309-2, Publisher: Nature Publishing Group.

[18] Wild Martin. The global energy balance as represented in CMIP6 climate models. Clim Dyn 2020;55(3):553–77. http://dx.doi.org/10.1007/s00382-020-05282-7.

[19] Pincus Robert, Mlawer Eli J, Delamere Jennifer S. Balancing accuracy, efficiency, and flexibility in radiation calculations for dynamical models. J Adv Model Earth Syst 2019;11(10):3074–89. http://dx.doi.org/10.1029/2019MS001621, URL https://onlinelibrary.wiley.com/doi/abs/10.1029/2019MS001621, _eprint: https://onlinelibrary.wiley.com/doi/pdf/10.1029/2019MS001621.

[20] Aumann Hartmut H, Chen Xiuhong, Fishbein Evan, Geer Alan, Havemann Stephan, Huang Xianglei, Liu Xu, Liuzzi Giuliano, DeSouza-Machado Sergio, Manning Evan M, Masiello Guido, Matricardi Marco, Moradi Isaac, Natraj Vijay, Serio Carmine, Strow Larrabee, Vidot Jerome, Chris Wilson R, Wu Wan, Yang Qiguang, Yung Yuk L. Evaluation of radiative transfer models with clouds. J Geophys Res: Atmospheres 2018;123(11):6142–57. http://dx.doi.org/10.1029/2017JD028063, URL https://onlinelibrary.wiley.com/doi/abs/10.1029/2017JD028063, _eprint: https://onlinelibrary.wiley.com/doi/pdf/10.1029/2017JD028063.

[21] Alvarado MJ, Payne VH, Mlawer EJ, Uymin G, Shephard MW, Cady-Pereira KE, Delamere JS, Moncet J-L. Performance of the line-by-line radiative transfer model (LBLRTM) for temperature, water vapor, and trace gas retrievals: recent updates evaluated with IASI case studies. Atmospheric Chem Phys 2013;13(14):6687–711. http://dx.doi.org/10.5194/acp-13-6687-2013, URL https://acp.copernicus.org/articles/13/6687/2013/, Publisher: Copernicus GmbH.

[22] Rodgers Clive D. Inverse methods for atmospheric sounding: theory and practice. Series on atmospheric oceanic and planetary physics, reprinted ed.. Vol. 2, Singapore: World Scientific; 2004, OCLC: 254137862.

[23] Iacono Michael J, Mlawer Eli J, Clough Shepard A, Morcrette Jean-Jacques. Impact of an improved longwave radiation model, RRTM, on the energy budget and thermodynamic properties of the NCAR community climate model, CCM3. J Geophys Res: Atmospheres 2000;105(D11):14873–90. http://dx.doi.org/10.1029/2000JD900091, URL https://onlinelibrary.wiley.com/doi/abs/10.1029/2000JD900091 _eprint: https://onlinelibrary.wiley.com/doi/pdf/10.1029/2000JD900091.

[24] Wu Yi, An Jingjing, Gui Chenxi, Xiao Chan, Yan Da. A global typical meteorological year (TMY) database on ERA5 dataset. Build Simul 2023;16(6):1013–26. http://dx.doi.org/10.1007/s12273-023-1015-3.

[25] Vilà Roger, Medrano Marc, Castell Albert. Climate change influences in the determination of the maximum power potential of radiative cooling. Evolution and seasonal study in Europe. Renew Energy 2023;212:500–13. http://dx.doi.org/10.1016/j.renene.2023.05.083, URL https://www.sciencedirect.com/science/article/pii/S0960148123007127.

[26] Fabiani Claudia, Muscio Alberto, Pisello Anna Laura. Introducing the enhanced solar reflectance index (SRI*) for comprehensive evaluation of spectrally selective cool materials in real-world scenarios. Sustain Energy Technol Assess 2025;81:104415. http://dx.doi.org/10.1016/j.seta.2025.104415, URL https://www.sciencedirect.com/science/article/pii/S2213138825002462.

[27] Bu Fan, Yan Da, Tan Gang, An Jingjing. A novel approach based on equivalent sky radiative temperature for quick computation of radiative cooling in building energy simulation. Renew Energy 2024;221:119820. http://dx.doi.org/10.1016/j.renene.2023.119820, URL https://www.sciencedirect.com/science/article/pii/S0960148123017354.

[28] Evangelisti Luca, Guattari Claudia, Asdrubali Francesco. On the sky temperature models and their influence on buildings energy performance: A critical review. Energy Build 2019;183:607–25. http://dx.doi.org/10.1016/j.enbuild.2018.11.037, URL https://www.sciencedirect.com/science/article/pii/S0378778818324605.

[29] Mandal Jyotirmoy, Huang Xin, Raman Aaswath P. Accurately quantifying Clear-Sky radiative cooling potentials: A temperature correction to the transmittance-based approximation. Atmosphere 2021;12(9). http://dx.doi.org/10.3390/atmos12091195, URL https://www.mdpi.com/2073-4433/12/9/1195.

[30] Jin Yeonghoon, Kats Mikhail. A gradient atmospheric model reveals enhanced radiative cooling potential and demonstrates the advantages of broadband emitters. Laser Photon Rev 2025;e00371.

[31] Mlawer Eli J, Taubman Steven J, Brown Patrick D, Iacono Michael J, Clough Shepard A. Radiative transfer for inhomogeneous atmospheres: RRTM, a validated correlated-k model for the longwave. J Geophys Res: Atmospheres 1997;102(D14):16663–82. http://dx.doi.org/10.1029/97JD00237, URL https://agupubs.onlinelibrary.wiley.com/doi/abs/10.1029/97JD00237 _eprint: https://agupubs.onlinelibrary.wiley.com/doi/pdf/10.1029/97JD00237.

[32] AER-RC. RRTM_LW. 2023, URL https://github.com/AER-RC/RRTM_LW, Original-date: 2020-12-15T20:32:26Z.

[33] 21GRD03 PaRaMetriC. 21GRD03 Parametric, metrological framework for passive radiative cooling technologies. 2025, URL https://parametric.inrim.it/.

[34] Belotti Claudio, Pattelli Lorenzo. PASTICHE, the PaRaMetriC atmospheric spectral tool for irradiance calculation using hourly ERA5 data. 2025, URL https://github.com/21grd03-parametric/pastiche/.

[35] Liou Kuo-Nan. An introduction to atmospheric radiation. International geophysics series, 2nd ed.. vol. 84, Amsterdam ; Boston: Academic Press; 2002.

[36] Remedios JJ, Leigh RJ, Waterfall AM, Moore DP, Sembhi H, Parkes I, Greenhough J, Chipperfield MP, Hauglustaine D. MIPAS reference atmospheres and comparisons to V4.61/V4.62 MIPAS level 2 geophysical data sets. Atmospheric Chem Phys Discuss 2007;7(4):9973–10017. http://dx.doi.org/10.5194/acpd-7-9973-2007, URL https://acp.copernicus.org/preprints/7/9973/2007/, Publisher: Copernicus GmbH.

[37] University of Wisconsin Space Science and Engineering Center (UW SSEC). Atmospheric emitted radiance interferometer (AERI). 2025, URL https://www.ssec.wisc.edu/aeri/.

[38] Knuteson RO, Best FA, DeSlover DH, Osborne BJ, Revercomb HE, Smith WL. Infrared land surface remote sensing using high spectral resolution aircraft observations. Adv Space Res 2004;33(7):1114–9. http://dx.doi.org/10.1016/S0273-1177(03)00752-X, URL https://www.sciencedirect.com/science/article/pii/S027311770300752X.

[39] Harries J, Carli B, Rizzi R, Serio C, Mlynczak M, Palchetti L, Maestri T, Brindley H, Masiello G. The Far-infrared Earth. Rev Geophys 2008;46(4). http://dx.doi.org/10.1029/2007RG000233, URL https://agupubs.onlinelibrary.wiley.com/doi/abs/10.1029/2007RG000233 _eprint: https://agupubs.onlinelibrary.wiley.com/doi/pdf/10.1029/2007RG000233.

[40] Sussmann R, Reichert A, Rettinger M. The Zugspitze radiative closure experiment for quantifying water vapor absorption over the terrestrial and solar infrared – Part 1: Setup, uncertainty analysis, and assessment of far-infrared water vapor continuum. Atmospheric Chem Phys 2016;16(18):11649–69. http://dx.doi.org/10.5194/acp-16-11649-2016, URL https://acp.copernicus.org/articles/16/11649/2016/.

[41] Hersbach Hans, Bell Bill, Berrisford Paul, Hirahara Shoji, Horányi András, Muñoz-Sabater Joaquín, Nicolas Julien, Peubey Carole, Radu Raluca, Schepers Dinand, Simmons Adrian, Soci Cornel, Abdalla Saleh, Abellan Xavier, Balsamo Gianpaolo, Bechtold Peter, Biavati Gionata, Bidlot Jean, Bonavita Massimo, De Chiara Giovanna, Dahlgren Per, Dee Dick, Diamantakis Michail, Dragani Rossana, Flemming Johannes, Forbes Richard, Fuentes Manuel, Geer Alan, Haimberger Leo, Healy Sean, Hogan Robin J, Hólm Elías, Janisková Marta, Keeley Sarah, Laloyaux Patrick, Lopez Philippe, Lupu Cristina, Radnoti Gabor, de Rosnay Patricia, Rozum Iryna, Vamborg Freja, Villaume Sebastien, Thépaut Jean-Noël. The ERA5 global reanalysis. Q J R Meteorol Soc 2020;146(730):1999–2049. http://dx.doi.org/10.1002/qj.3803, URL https://onlinelibrary.wiley.com/doi/abs/10.1002/qj.3803 _eprint: https://onlinelibrary.wiley.com/doi/pdf/10.1002/qj.3803.

[42] Talagrand Olivier. Variational assimilation. In: Lahoz William, Khattatov Boris, Menard Richard, editors. Data assimilation: making sense of observations. Berlin, Heidelberg: Springer; 2010, p. 41–67. http://dx.doi.org/10.1007/978-3-540-74703-1_3.

[43] Parker Wendy S. Reanalyses and observations: What's the difference? Bull Am Meteorol Soc 2016;97(9):1565–72. http://dx.doi.org/10.1175/BAMS-D-14-00226.1, URL https://journals.ametsoc.org/view/journals/bams/97/9/bams-d-14-00226.1.xml, Publisher: American Meteorological Society Section: Bulletin of the American Meteorological Society.

[44] Copernicus Climate Change Service. ERA5 hourly data on pressure levels from 1940 to present. 2018, URL https://cds.climate.copernicus.eu/doi/10.24381/cds.bd0915c6.

[45] Copernicus Climate Change Service. ERA5 hourly data on single levels from 1940 to present. 2018, URL https://cds.climate.copernicus.eu/doi/10.24381/cds.adbb2d47.

[46] Calvin Katherine, Dasgupta Dipak, Krinner Gerhard, Mukherji Aditi, Thorne Peter W, Trisos Christopher, Romero José, Aldunce Paulina, Barrett Ko, Blanco Gabriel, Cheung William WL, Connors Sarah, Denton Fatima, Diongue-Niang Aïda, Dodman David, Garschagen Matthias, Geden Oliver, Hayward Bronwyn, Jones Christopher, Jotzo Frank, Krug Thelma, Lasco Rodel, Lee Yune-Yi, Masson-Delmotte Valérie, Meinshausen Malte, Mintenbeck Katja, Mokssit Abdalah, Otto Friederike EL, Pathak Minal, Pirani Anna, Poloczanska Elvira, Pörtner Hans-Otto, Revi Aromar, Roberts Debra C, Roy Joyashree, Ruane Alex C, Skea Jim, Shukla Priyadarshi R, Slade Raphael, Slangen Aimée, Sokona Youba, Sörensson Anna A, Tignor Melinda, Van Vuuren Detlef, Wei Yi-Ming, Winkler Harald, Zhai Panmao, Zommers Zinta, Hourcade Jean-Charles, Johnson Francis X, Pachauri Shonali, Simpson Nicholas P, Singh Chandni, Thomas Adelle, Totin Edmond, Arias Paola, Bustamante Mercedes, Elgizouli Ismail, Flato Gregory, Howden Mark, Méndez-Vallejo Carlos, Pereira Joy Jacqueline, Pichs-Madruga Ramón, Rose Steven K, Saheb Yamina, Sánchez Rodríguez Roberto, Ürge-Vorsatz Diana, Xiao Cunde, Yassaa Noureddine, Alegría Andrés, Armour Kyle, Bednar-Friedl Birgit, Blok Kornelis, Cissé Guéladio, Dentener Frank, Eriksen Siri, Fischer Erich, Garner Gregory, Guivarch Céline, Haasnoot Marjolijn, Hansen Gerrit, Hauser Mathias, Hawkins Ed, Hermans Tim, Kopp Robert, Leprince-Ringuet Noëmie, Lewis Jared, Ley Debora, Ludden Chloé, Niamir Leila, Nicholls Zebedee, Some Shreya, Szopa Sophie, Trewin Blair, Van Der Wijst Kaj-Ivar, Winter Gundula, Witting Maximilian, Birt Arlene, Ha Meeyoung, Romero José, Kim Jinmi, Haites Erik F, Jung Yonghun, Stavins Robert, Birt Arlene, Ha Meeyoung, Orendain Dan Jezreel A, Ignon Lance, Park Semin, Park Youngin, Reisinger Andy, Cammaramo Diego, Fischlin Andreas, Fuglestvedt Jan S, Hansen Gerrit, Ludden Chloé, Masson-Delmotte Valérie, Matthews JB Robin, Mintenbeck Katja, Pirani Anna, Poloczanska Elvira, Leprince-Ringuet Noëmie, Péan Clotilde. In: Core Writing Team H Lee, Romero J, editors. IPCC, 2023: Climate change 2023: Synthesis report. Contribution of working groups I, II and III to the sixth assessment report of the intergovernmental panel on climate change. Technical report, Geneva, Switzerland: IPCC, Intergovernmental Panel on Climate Change (IPCC); 2023, URL https://www.ipcc.ch/report/ar6/syr/, Edition: First.

[47] ISO 15927-4:2005(E). Hygrothermal performance of buildings — Calculation and presentation of climatic data — Part 4: Hourly data for assessing the annual energy use for heating and cooling. Standard, Geneva, CH: International Organization for Standardization; 2005, Volume: 2005.

[48] Huld Thomas. Typical Meteorological Data access service. 2017, URL http://data.europa.eu/89h/jrc-tmy-tmy-download-service, Publisher: European Commission, Joint Research Centre (JRC).

[49] Siegel Robert, Howell John, Mengüç M Pinar. Thermal radiation heat transfer. CRC Press; 2011.

[50] Manara Jochen, Hartmann Jürgen, Kerwagen Fabian, Maack Christoph, Muscio Alberto, Paeth Heiko, Ebert Hans-Peter. Passive radiative cooling materials with special focus on the reduction of urban heat island effect: A current summarized classification of need, approaches and characterization methods. Int J Thermophys 2025;46. http://dx.doi.org/10.1007/s10765-025-03529-1.

[51] Sharples S, Charlesworth PS. Full-scale measurements of wind-induced convective heat transfer from a roof-mounted flat plate solar collector. Sol Energy 1998;62(2):69–77. http://dx.doi.org/10.1016/S0038-092X(97)00119-9, URL https://www.sciencedirect.com/science/article/pii/S0038092X97001199.

[52] Manara Jochen, Arduini Mariacarla, Hanssen Leonard. Integrating sphere reflectance and transmittance intercomparison measurements for evaluating the accuracies of the achieved results. High Temp - High Press 2009;38:259–76.

[53] DIN EN 12898:2019-06. Glass in building - Determination of the emissivity. 2019.

[54] DIN EN 410:2011-04. Lass in building - Determination of luminous and solar characteristics of glazing. 2011, http://dx.doi.org/10.31030/1747600.

[55] Zenodo. 21Grd03 parametric. 2025, URL https://zenodo-rdm.web.cern.ch/communities/21grd03-parametric/records.

[56] Clough SA, Shephard MW, Mlawer EJ, Delamere JS, Iacono MJ, Cady-Pereira K, Boukabara S, Brown PD. Atmospheric radiative transfer modeling: a summary of the AER codes. J Quant Spectrosc Radiat Transfer 2005;91(2):233–44. http://dx.doi.org/10.1016/j.jqsrt.2004.05.058, URL https://www.sciencedirect.com/science/article/pii/S0022407304002158.

[57] Stokes Gerald M, Schwartz Stephen E. The atmospheric radiation measurement (ARM) program: Programmatic background and design of the cloud and radiation test bed. Bull Am Meteorol Soc 1994;75(7):1201–22. http://dx.doi.org/10.1175/1520-0477(1994)075<1201:TARMPP>2.0.CO;2, URL https://journals.ametsoc.org/view/journals/bams/75/7/1520-0477_1994_075_1201_tarmpp_2_0_co_2.xml.

[58] Driemel A, Augustine J, Behrens K, Colle S, Cox C, Cuevas-Agulló E, Denn FM, Duprat T, Fukuda M, Grobe H, Haeffelin M, Hodges G, Hyett N, Ijima O, Kallis A, Knap W, Kustov V, Long CN, Longenecker D, Lupi A, Maturilli M, Mimouni M, Ntsangwane L, Ogihara H, Olano X, Olefs M, Omori M, Passamani L, Pereira EB, Schmithüsen H, Schumacher S, Sieger R, Tamlyn J, Vogt R, Vuilleumier L, Xia X, Ohmura A, König-Langlo G. Baseline surface radiation network (BSRN): structure and data description (1992–2017). Earth Syst Sci Data 2018;10(3):1491–501. http://dx.doi.org/10.5194/essd-10-1491-2018, URL https://essd.copernicus.org/articles/10/1491/2018/.

[59] Morcrette J-J, Barker HW, Cole JNS, Iacono MJ, Pincus R. Impact of a new radiation package, mcrad, in the ECMWF integrated forecasting system. Mon Weather Rev 2008;136(12):4773–98. http://dx.doi.org/10.1175/2008MWR2363.1, URL https://journals.ametsoc.org/view/journals/mwre/136/12/2008mwr2363.1.xml.

[60] Hogan Robin J, Bozzo Alessio. A flexible and efficient radiation scheme for the ECMWF model. J Adv Model Earth Syst 2018;10(8):1990–2008. http://dx.doi.org/10.1029/2018MS001364, URL https://onlinelibrary.wiley.com/doi/abs/10.1029/2018MS001364 _eprint: https://onlinelibrary.wiley.com/doi/pdf/10.1029/2018MS001364.

[61] Bozzo Alessio, Benedetti Angela, Flemming Johannes, Kipling Zak, Rémy Samuel. An aerosol climatology for global models based on the tropospheric aerosol scheme in the integrated forecasting system of ECMWF. Geosci Model Dev 2020;13(3):1007–34. http://dx.doi.org/10.5194/gmd-13-1007-2020, URL https://gmd.copernicus.org/articles/13/1007/2020/, Publisher: Copernicus GmbH.

[62] Haeffelin Martial, Badosa Jordi. Basic measurements of radiation at station palaiseau (2003-06 et seq). 2022, URL https://doi.org/10.1594/PANGAEA.946383.

[63] Khorsandi Mostafa, St-Hilaire Andre, Arsenault Richard. Assessing the surface downward longwave irradiance models using ERA5 input data in Canada. J Hydrometeorol 2023;24(6):1175–90. http://dx.doi.org/10.1175/JHM-D-22-0184.1, URL https://journals.ametsoc.org/view/journals/hydr/24/6/JHM-D-22-0184.1.xml.

[64] Feng Chunjie, Zhang Xiaotong, Xu Jiawen, Yang Shuyue, Guan Shikang, Jia Kun, Yao Yunjun. Comprehensive assessment of global atmospheric downward longwave radiation in the state-of-the-art reanalysis using satellite and flux tower observations. Clim Dyn 2023;60(5):1495–521. http://dx.doi.org/10.1007/s00382-022-06366-2.

[65] Tang Wenjun, Qin Jun, Yang Kun, Zhu Fuxin, Zhou Xu. Does ERA5 outperform satellite products in estimating atmospheric downward longwave radiation at the surface? Atmos Res 2021;252:105453.

[66] Huang Guanghui, Li Xin, Huang Chunlin, Liu Shaomin, Ma Yanfei, Chen Hao. Representativeness errors of point-scale ground-based solar radiation measurements in the validation of remote sensing products. Remote Sens Environ 2016;181:198–206. http://dx.doi.org/10.1016/j.rse.2016.04.001, URL https://www.sciencedirect.com/science/article/pii/S003442571630147X.

[67] Adibekyan A, Schumacher J, Pattelli L, Manara J, Meriç S, Bazkir Ö, Cucchi C, Sprengard C, Pérez G, Campos J, Hameury J, Andersson A, Clausen S, Rasmussen A, Belotti C, Efthymiou S, Assimakopoulos M-N, Papadaki D, Manoocheri F, Llados A, Jaramillo-Fernandez J, Gionfini T, Ortisi M, Peter A, Kleinbub M, Bante J, Donath L, Herzog H, Monte C. Emissivity and reflectivity measurements for passive radiative cooling technologies. Int J Thermophys 2025;46(5):66. http://dx.doi.org/10.1007/s10765-025-03532-6.

[68] Pirvaram Atousa, Leung Siu Ning, O'Brien Paul G. The global warming potential of geoengineering via radiative cooling. Adv Sustain Syst 2025;9(5):2400948.